Advances in Aerodynamics

RESEARCH Open Access

High fidelity numerical simulations on the unsteady flow field of low-pressure turbine cascades with and without upstream disturbance at moderate Reynolds number

Hongbo Zhu[1], Xiyuan Pang[1], Feng Wu[2], Chunxiao Zhang[3], Yan Bao[1*] and Hui Xu[4*]

*Correspondence: ybao@sjtu.edu.cn; dr.hxu@sjtu.edu.cn
[1] School of Naval Architecture, Ocean and Civil Engineering, Shanghai Jiao Tong University, Shanghai 200240, China
[4] School of Aeronautics and Astronautics, Shanghai Jiao Tong University, Shanghai 200240, China
Full list of author information is available at the end of the article

Abstract

This paper numerically investigates the aerodynamic performance of the T106A low-pressure turbine based with different inflow conditions at moderate Reynolds number by using high performance computing based on high order unstructured methods. Two different inflow conditions respectively of uniform and disturbed are considered, while for the latter a small circular cylinder is placed upstream of the cascade to generate wake turbulence as a long-standing disturbance. A high order Fourier-spectral/*hp* element method is employed to solve the flow dynamics in the cascade of high complex geometries. Flow transition characteristics are quantified in terms of the distribution of cascade wall surface pressure and friction coefficient, the distribution of wake profile pressure loss and the evolution characteristics of boundary layer flow structures as well. The numerical results show that the current numerical simulations accurately predict the flow transition performance of low-pressure turbine cascades and capture the effects of wake-generated disturbance on the cascade, which is shown to effectively modify the flow transition performance as compared with the uniform inflow case.

Keywords: Fourier-spectral/*hp* element method, Low pressure turbine, Wake generated disturbance, Aerodynamic characteristics

1 Introduction

The low pressure turbine (LPT) is uniquely designed to provide high aerodynamic efficiency in low pressure ratio operation, to recover exhaust energy whilst minimizing back pressure. The flow past LPT is inherently unsteady because of the wake generated behind upstream blade rows. It is well documented that laminar-turbulent transition is responsible for the energy loss with various influential parameters, but the effects produced by wake dynamics of the upstream blade are essentially striking among them. Although considerable knowledge is already obtained in terms of the LPT flow with both the laminar and turbulent flow conditions, the flow over transitional region remains one of the

main challenges particularly when considering the wake passing effects of upstream blade rows.

Earlier studies on the influence of wake passing on boundary layer development were conducted by Pfeil et al. [1], who investigated how the wake generated by steel bars affects laminar to turbulent transition on a circular cylinder. Hodson [2] studied the impact of passing wakes on the loss generation process in a LPT and observed that wake passing significantly suppresses a laminar separation region. The physics behind laminar-turbulence transition was explored by Mayle [3], and found that turbulent intensity, pressure gradient and wake strength are fundamental factors associated with the wake passing. Halstead et al. [4] performed comprehensive tests on a large scale compressor and a LPT to explore the wake passing effects on the onset of transition and laminar separation bubble and the existence of the becalmed region. Stadtm and Fottner [5] presented a compilation of experimental data on the effects of wake-induced transition on a highly loaded LPT cascade. Although the underlying flow mechanism is not yet completely understood, the wake passing is confirmed to be beneficial and suggested to be considered in the design process of modern gas turbines. They further argued that for further optimizations, in the next step, one enables numerical simulations detailed enough to capture the major effects while being as uncomplicated as possible at the same time to be cost-effective.

The high-fidelity computational method can accurately identify the laminar-turbulent transition behavior, so that the flow transition simulation of simplified model based on high-performance computing has been reported recently in the community of computational fluid dynamics. However, due to the complex geometrical configuration and fluid dynamic environment of LPT blades with complex upstream wakes, so far, a question of how to accurately predict the LPT flow associated with the transition development is still not well resolved.

On the basis of numerical simulations, a few attempts have been made on the issue, but most of the simulations used are the finite difference method or finite volume method. For example, Sandberg et al. [6] and Michelassi et al. [7] developed a compact fourth-order finite difference scheme to simulate and analyze the influence of upstream turbulence on the aerodynamic performance of the cascade; Rai et al. [8] adopted a higher-order upwind scheme to predict the flow transition of low-pressure turbine blades. Spectral/*hp* finite element method has attracted much attention in recent years and it has been widely used in solving incompressible and compressible flows [9–11]. More recently, Nakhchi et al. [12] investigates the secondary vortex flows over an oscillating T106A blade using a direct numerical simulation (DNS) method based on spectral/*hp* element method. The method employs high-degree piecewise polynomial basis functions which results in a very high-order finite element approach. The results show that the blade oscillation can significantly influence the transitional flow structure and the wake profile. However, the application of high-order spectral element method for the aerodynamic performance of low-pressure turbine cascades subject to incoming wake in the transition regime has not been reported so far.

It should be noted that most work reported in the literature about the wake passing effects on LTP flow focuses their attention on periodicity of incoming wakes. For example, Wu & Durbin [13] simulated the flow in the T106 cascade subject to periodically

incoming wakes generated by moving cylinder. By DNS simulations, Wissink [14] reported that the impinging wakes induce the formation of longitudinal vortices along the pressure side of the turbine blade. In the center of the passage between the blades, the wake is severely deformed as a consequence of straining and stretching by the free-stream flow. However, a fundamental question of what are the long-lasting effects of flow disturbance from the upstream wake, which is fixed rather than periodically passing, is still open to the community in this area.

In this paper, a high-order Fourier-spectral element method is employed to perform the numerical analysis on the unsteady flow field of low-pressure turbine cascades with and without upstream wake at moderate Reynolds number conditions to evaluate its capability for prediction of complex transitional flow behavior in the boundary layer of LPT. This paper is organized as follows: In Section 2, the selected numerical methods are introduced in detail; in Section 3, the physical model is described with the numerical setting introduced; in Section 4, the aerodynamic performance of T106A low-pressure turbine blade under two kinds of inflow conditions is quantitatively analyzed; finally, the conclusions are summarized in Section 5.

2 Numerical method

The Navier-Stokes equations are used to describe the flow dynamics and written in non-dimensional form as follows,

$$\frac{\partial \mathbf{u}}{\partial t} + \mathbf{u} \bullet \nabla \mathbf{u} = -\nabla p + \frac{1}{Re}\nabla^2 \mathbf{u} \tag{1}$$

$$\nabla \bullet \mathbf{u} = 0 \tag{2}$$

where $\mathbf{u}$ and p are the velocity and the pressure, respectively. $Re = U_\infty C/v$ is the Reynolds number based on the uniform current at the inlet (here, v is the kinematic viscosity of incoming flow and C is the chord length as depicted in Fig. 1). ∇ is the gradient operator in the inertial coordinate system. The spanwise evolution of the flow is resolved by introducing Fourier expansion as the discretisation for the spanwise direction because the flow configuration possesses a spatial homogeneity in this direction. The 2D computational domain is therefore discretized into quadrilateral elements and the high-order modified Jacobian tensor-product polynomial shape functions are subsequently imposed on each macro-element. The spatial resolution is controlled by varying the order of polynomial expansion, which is interpolated at the Gauss-Lobatto-Legendre quadrature points [15]. A stiffly stable high-order splitting scheme proposed by Karniadakis et al. [16], which is also referred to as a velocity correction scheme [17], is employed for time integration of the Navier–Stokes equations. The details about this method can refer to Karniadakis and Sherwin [18].

3 Physical model and numerical set-up

The physical model considered is a representative industrial LPT cascade with two different incoming flows, as shown in Fig. 1. While uniform inflow condition is considered in the case I, wake flow behind a small cylinder is generated upstream of the

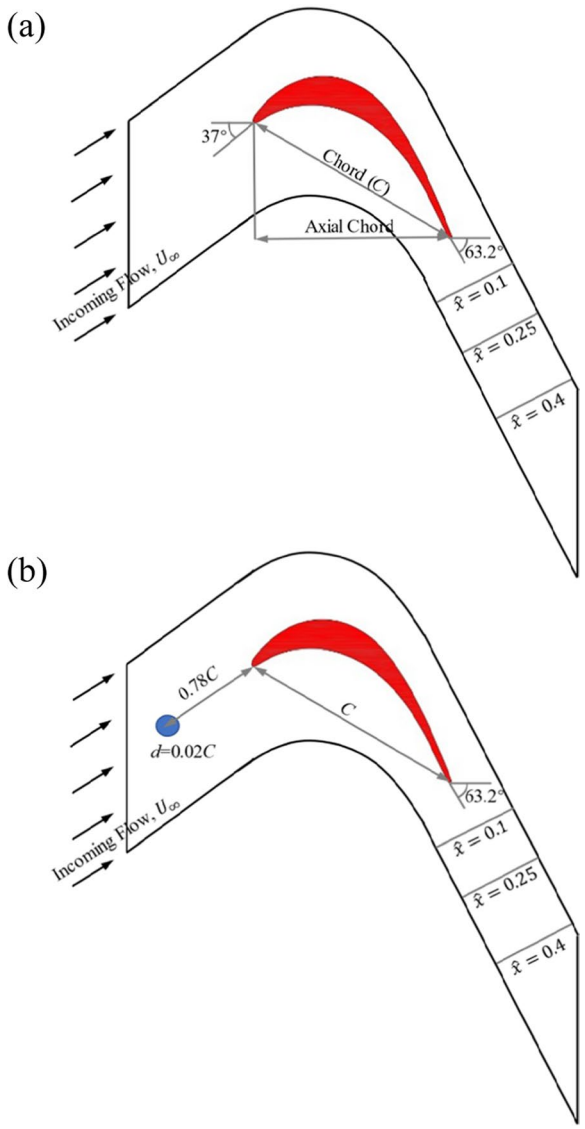

Fig. 1 Schematic diagram of T106A LPT cascade: (**a**) Case I under uniform inflow condition and (**b**) Case II under incoming disturbed inflow condition

cascade as a wake-type disturbance in the case II. A moderate inflow Reynolds number of $Re_\infty = 50{,}000$ (based on inflow velocity $U_\infty = 1$ and chord $C = 1$) is employed, which corresponds approximately to $Re_2 = 88{,}450$ (based on the mixed-out velocity magnitude at the exit measurement plane).

The inflow plane is situated $1.0C_{ax}$ upstream of the leading edge (LE) for the case I, whereas this plane is further moved a distance of $0.5C_{ax}$ towards upstream direction for the case II. The small cylinder in the case II is located $0.78C$ upstream from the LE and its diameter is fixed to be $0.02C$, therefore the corresponding Reynolds number based on the cylinder diameter is $Re_d = 1000$, which ensures the cylinder wake is fully developed into a regime of turbulence. High order outflow conditions [19] are applied to the outflow plane, located $1.5C_{ax}$ downstream of the trailing

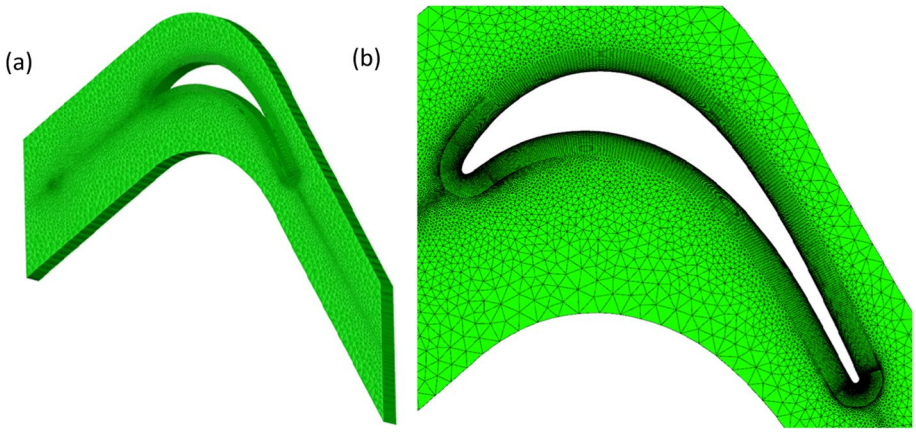

Fig. 2 Mesh of disturbed case II: (**a**) macroscopic finite element grid distribution of computational domain and (**b**) zoomed in grid near the blade wall

edge (TE), while periodic conditions are enforced in the pitchwise and spanwise directions.

The Gmsh software [20] is employed for mesh generation and the mesh used for case II consists of 20,460 quadrilateral elements in the O-mesh around the solid wall of the LTP and 19,002 triangular elements in the unstructured part in the domain away from the wall, as shown in Fig. 2. The micro-element mesh resolution for the case I is similar to that for case II. A number of 1324 mesh points is non-uniformly distributed along the wall surface, which resulted in a $\Delta s^+ = 0.643$ - 6.978. A number of 61 points is distributed along wall-normal direction in the O-mesh domain, and the corresponding Δy^+ value along the blade surface is ranged from 0.06 to 6.5. With close to the trailing edge, where flow transition is expected to happen, the Δy^+ value is less than 1. The spanwise domain is extended for $L_z = 0.2C$ and resolved with $N_z = 96$ Fourier planes. The resolution obtained in the directions along the blade surface, normal to the blade and in the spanwise direction is within typical limits recommended for DNS [21], suggesting that the turbulent scales of interest can be captured in the current simulations. Following the numerical stabilization technique used in [22], for the exponential kernel of SVV in the spanwise direction, a diffusion coefficient and cutoff ratio are set to a value of 1.0 and 0.6, respectively.

4 Results and discussion

4.1 Pressure and friction on the wall surface

A first comparison of the aerodynamic performance of T106A cascade is quantified by the analysis of the time- and spanwise-averaged pressure coefficient and skin friction coefficients. The static pressure coefficient C_p is defined as: $C_p = (p - p_2)/(p_{t1} - p_2)$, where p, p_{t1}, and p_2 stand for the static pressure on the blade surface, the total inlet pressure and the outlet static pressure, respectively. Figure 3 shows the results subject to uniform and disturbed inflow for the case I and case II with the comparison of the results from Cassinelli et al. [23]. As can be seen from the simulation results of the time-averaged C_p distribution in Fig. 3(a), both uniform inflow

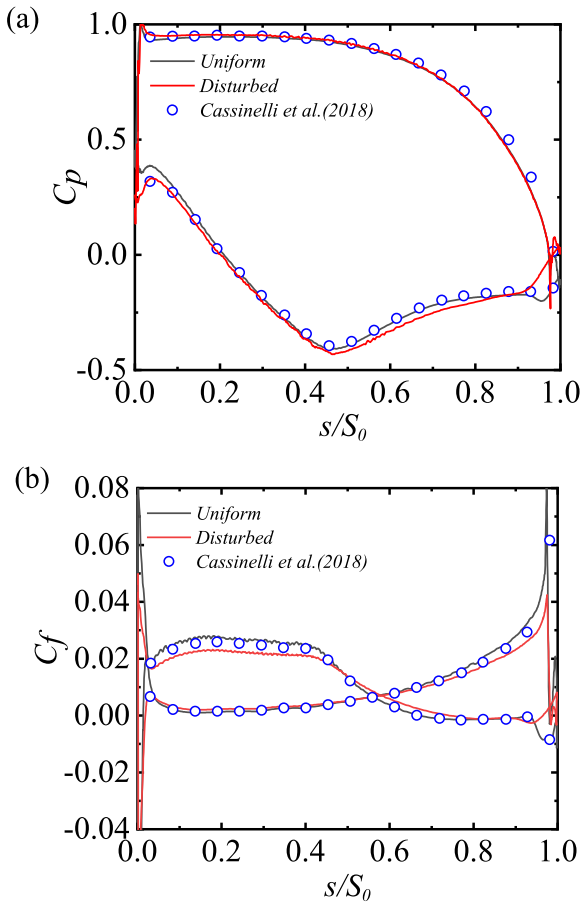

Fig. 3 The distribution of time- and spanwise-averaged (**a**) static pressure coefficient and (**b**) surface friction coefficient

and disturbed inflow obtain a similar pressure distribution along the pressure surface. It implies that the wake-type disturbance by such a small cylinder has negligible impact on the pressure side of the blade. As flow is developed along the suction surface towards the trailing edge, the pressure for the case I is gradually decreased in the presence of the favorable pressure gradient, and the pressure is changed into suction near the position where $s/S_0 \approx 0.2$. The pressure coefficient of the suction surface is rising toward the trailing edge after reaching a trough value at $s/S_0 \approx 0.456$. The pressure plateau that appears near the trailing edge indicates that separation occurs in the boundary layer and a separation bubble is formed. The results obtained from the present work are in good agreement with the numerical results reported by Cassinelli et al. [23], with only minor differences in the aft portion of pressure surface. It can be seen that the difference of the static pressure coefficient under different inflow conditions is mainly reflected around the leading edge and trailing edge of the suction surface, but has little influence on the middle part of the suction surface. For the rear side of the suction surface, the pressure on the blade surface recovers rapidly and the pressure platform disappears when the wake-type disturbance exists upstream. On

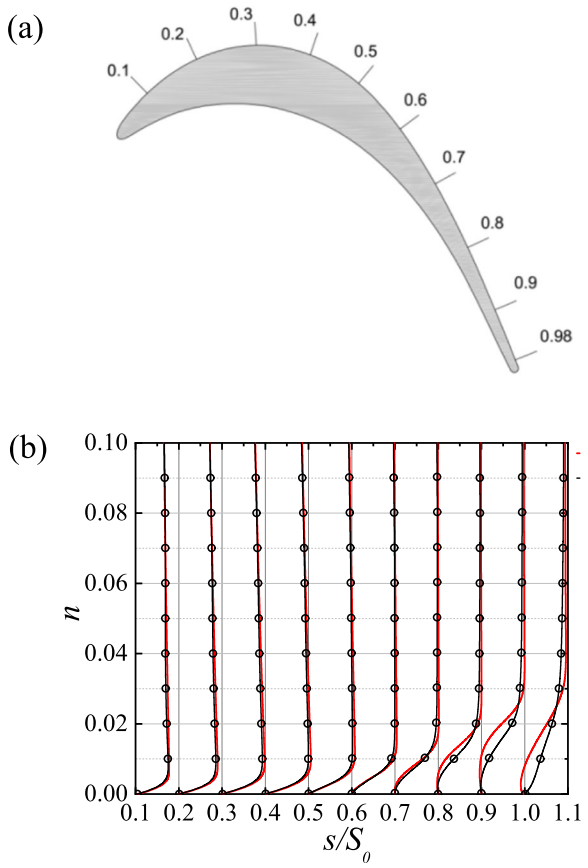

Fig. 4 (**a**) Typical locations on the suction side of the blade and (**b**) Boundary layer profiles for uniform and disturbed incoming flow conditions (solid lines: uniform inflow and circle-dot lines: disturbed inflow)

the other hand, the upstream wake-disturbance slightly reduces the pressure on the front portion particularly close to the leading edge.

The skin-friction coefficient of blade is defined as $C_f = \tau_w/\left(0.5\rho U_\infty^2\right)$, and its distribution along the suction and pressure surfaces is shown in Fig. 3(b). For the case I, good agreement is observed in the distribution trend of C_f as compared with Cassinelli et al. [23]. For the case II, the skin friction coefficient is distorted along the whole blade on both suction and pressure surface. A small secondary recirculation bubble found at $s/S_0 \approx 0.95$ in the uniform inflow case, which is well matched again with Cassinelli et al. [23], is disappeared in the disturbed inflow. The incoming flow with disturbances energizes the boundary layer of the blade, which leads to an anticipated reattachment of the separated boundary layer before the trailing edge. This can be proved in the observation that the sign of C_f is changed from negative to positive near the trailing edge as compared to the uniform inflow case I. The disturbed inflow also modifies the C_f distribution along the front portion of the blade with respect to the uniform case I. In particular, the magnitude of C_f is decreased in the front portion where favorable pressure gradient dominates the boundary layer. The reason is probably that the impingement and stretching of streamwise vortices introduces significant reducing of pressure on the leading edge of the blade as evidenced in Fig. 3(a).

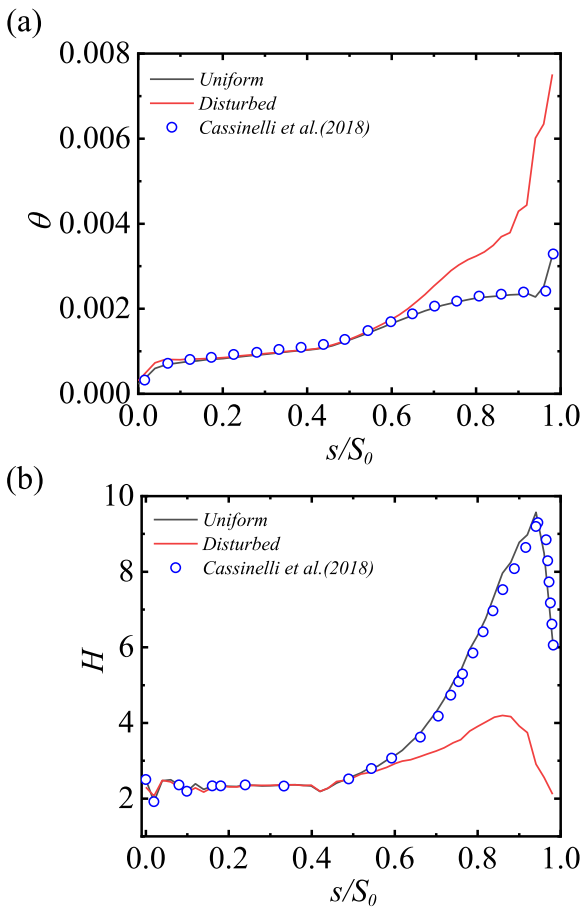

Fig. 5 (**a**) Time-averaged momentum thickness distribution comparison; (**b**) Time-averaged shape factor comparison

4.2 Boundary layer characteristics

The time- and spanwise-averaged boundary layer profiles from case I and case II are compared in Fig. 4. Ten points were selected along the suction surface of the cascade between $s/S_0 = 0.1 \sim 0.98$ and the tangential velocity profile at each point was plotted with the perpendicular coordinate n. The profiles match well before $s/S_0 = 0.60$, but it starts to deviate from each other at $s/S_0 = 0.70$ and becomes more visible at larger s/S_0. The boundary layer is detected to be more energetic when it is close to the trailing edge for the case of disturbed inflow as compared with that for the case of uniform inflow. An injection of extra momentum into the boundary layer therefore results in a shortening of separation bubble and reattachment again before the trailing edge, which is in-line with the friction coefficient behavior as shown in Fig. 3(b).

The parameters such as shape factor, H, and momentum thickness, θ, highly reflect the evolution characteristics of boundary layer of the turbine blade and are linked to profile loss estimation [24]. Figure 5 shows their distributions along the suction surface of the blade, with the inclusion of the results in Cassinelli et al. [23]. When $s/S_0 < 0.4$, the shape factor shows a plateau shape around a value of 2.5, verifying the nature of laminar state in the front portion of the boundary layer. After this point, its value increases

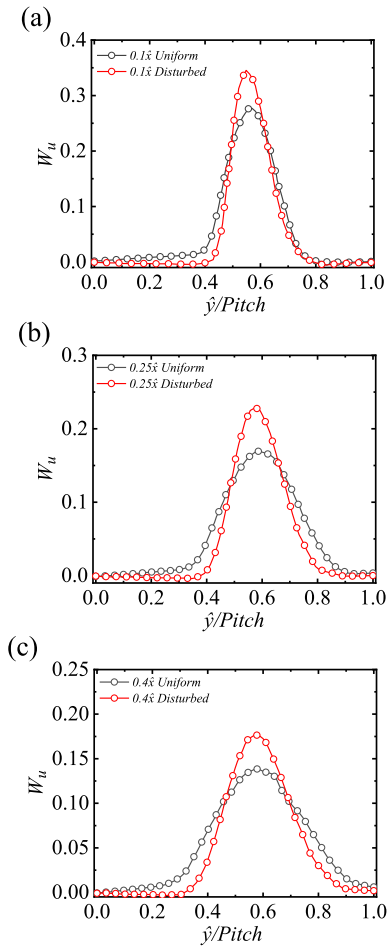

Fig. 6 Wake pressure loss coefficient at (**a**) $\hat{x} = 0.1$; (**b**) $\hat{x} = 0.25$ and (**c**) $\hat{x} = 0.4$

gradually along the suction surface and reaches a peak at around $s/S_0 = 0.94$, and then a dramatic jump is evidenced for further increase in s/S_0, which indicates that flow transition is triggered in the aft portion of the boundary layer. However, the value of shape factor is still greater than 6 at the trailing edge, illustrating that the transition to turbulence is not completed in the boundary layer at this *Re*. Some numerical oscillations are observed at lower polynomial order in the results in Cassinelli et al. [23], however the current predictions at the same polynomial order match well with the results at higher polynomial order in Cassinelli et al. [23]. The reason is mainly due to the high resolution of micro-element used in our simulations. The momentum thickness distribution shows an increasing trend along the suction surface, which is again in good agreement with the results from Cassinelli et al. [23].

The presence of a small cylinder upstream introduces striking modification in the evolution of these statistics of boundary layer. Since the cylinder's wake increases the turbulence intensity of incoming flow, the momentum thickness increases rapidly after $s/S_0 = 0.54$, so that the shape factor does not surge due to the rapid increase of the boundary layer thickness after separation, and the boundary layer velocity profile is fuller, which has a suppressive effect on the boundary layer separation. At the same time, we can see

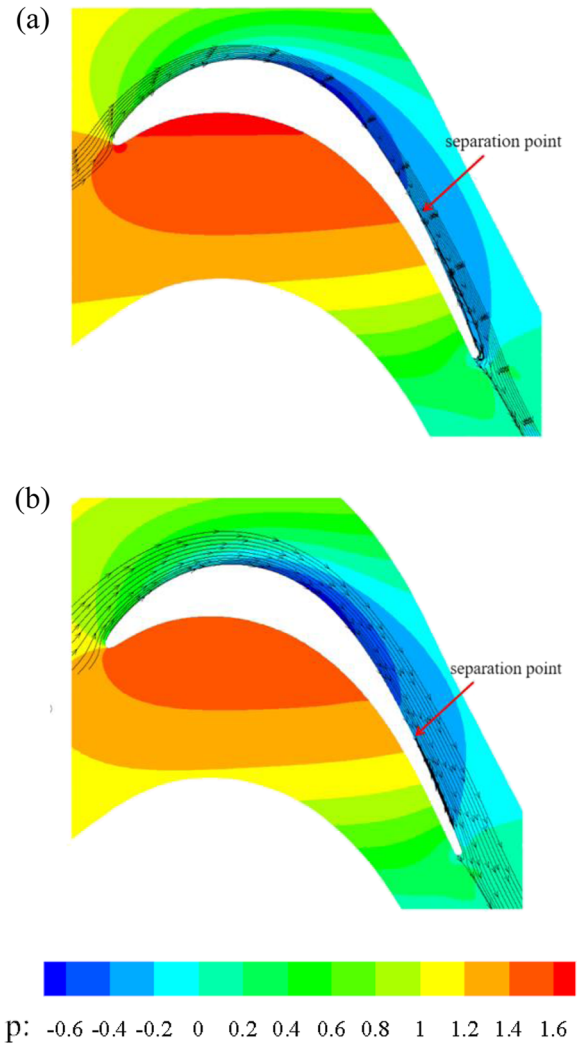

Fig. 7 Time-averaged streamline and pressure contour: (**a**) uniform inflow condition; (**b**) disturbed inflow condition

that the shape factor at the trailing edge of the blade suction surface has dropped to 2 under the disturbed inflow condition, indicating that the boundary layer has basically completed the transition when the blade is subject to wake inflow turbulence.

4.3 Wake profiles

The normalized distance from the trailing edge is defined as $\hat{x} = (x - x_{TE})/C_{ax}$, which is depicted in Fig. 1. The profiles of wake pressure loss coefficient, which is defined as $W_u = (p_{t1} - p_{t2})/(p_{t1} - p_2)$ (where p_{t1} is the spanwise averaged total pressure at the inlet, p_{t2} is the spanwise averaged total pressure at the outlet, and p_2 is the spanwise averaged static pressure at the outlet), are extracted by interpolating the time-averaged pressure fields from the unstructured mesh to traverses of equispaced points in the pitchwise direction; three extraction planes with streamwise locations $\hat{x} = 0.1$, 0.25, 0.4 are

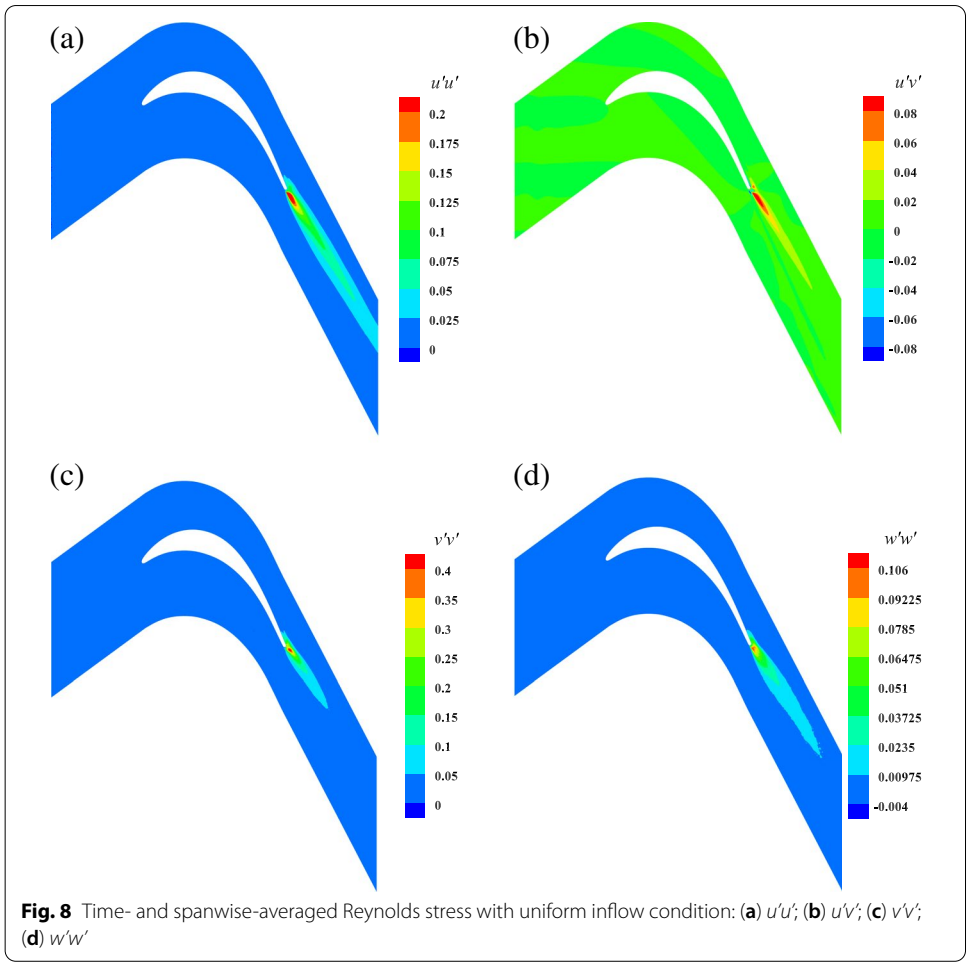

Fig. 8 Time- and spanwise-averaged Reynolds stress with uniform inflow condition: (**a**) *u′u′*; (**b**) *u′v′*; (**c**) *v′v′*; (**d**) *w′w′*

analyzed in Fig. 6. It can be seen that the pressure loss near the wake of the cascade is very obvious under the condition of both uniform and disturbed inflows. The center of the wake moves to the side of the suction surface. This is due to the existence of separation bubbles at the rear of the suction surface. At $\hat{x} = 0.1$, the peak deficit reaches the maximum value. As $\hat{x}$ increases, the loss coefficient decreases and the width of corresponding wake increases. A similar trend is detected for the case with disturbed inflow at the measured wake positions. More importantly, it is also noticed that the pressure loss is visibly reduced for the disturbed inflow case as compared with that for the uniform inflow case.

In Fig. 7(a) and (b), we compare the time- and spanwise-averaged pressure contour of the cascade under uniform inflow and disturbed inflow conditions. The streamline is also given in this image. From the comparison, we can notice that the presence of the small cylinder alternates the pressure field around the blade surface. In particular, the wake momentum deficit behind the small cylinder slightly reduces the pressure magnitude along the pressure surface and the front portion of the suction surface of the blade. Rising up of the pressure around the trailing edge is also visible in this figure, which is consistent with the pressure coefficient shown in Fig. 3(a). The streamline with the marked separation point in the figure shows the formation of the separation bubble on the aft

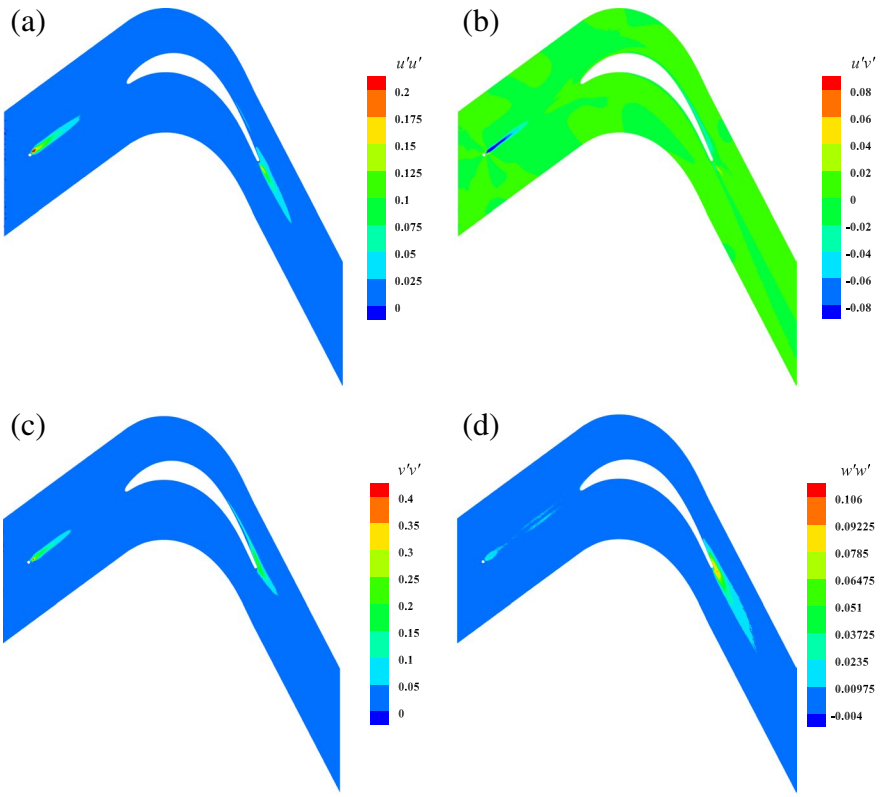

Fig. 9 Time- and spanwise-averaged Reynolds stress with disturbed inflow condition: (**a**) *u'u'*; (**b**) *u'v'*; (**c**) *v'v'*; (d) *w'w'*

portion of the blade, which looks significantly shorter in closed shape in the disturbed inflow case as compared with that in the uniform inflow case, which is again in-line with the variation of the skin friction coefficient shown in Fig. 3(b).

Figures 8 and 9 show the time- and spanwise-averaged Reynolds stress contours in the cascade channel for the uniform inflow and disturbed inflow cases, respectively.

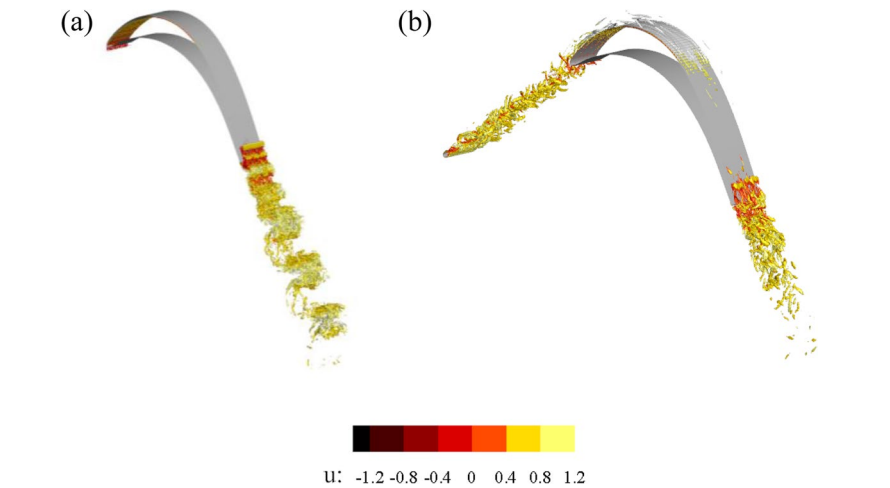

Fig. 10 Instantaneous isosurfaces of Q-contoured by velocity magnitude: (**a**) uniform inflow; (**b**) disturbed inflow

For uniform flow case, Reynolds normal stresses occur in the shear layer behind the suction surface of the cascade and reach maximum values in the wake region of the blade. Except for the shear layer behind the suction surface and the wake region of the blade, the Reynolds normal stresses in other places are close to zero. While in disturbed case, due to the high turbulence intensity and strong velocity pulsation of the cylinder's wake, there are also large Reynolds normal stress values in the strip region behind the cylinder. The influence of this phenomenon is that the position of Reynolds stress in the boundary layer behind the suction surface begins to increase in advance, the area of high Reynolds stress is closer to the cascade surface, the wake is filled with fully developed turbulence, and the area of high pulsation increases. For Reynolds shear stress, since the magnitudes of $u'w'$ and $v'w'$ are small, we only analyze for $u'v'$. It can be seen that, compared to the uniform flow case, the $u'v'$ values of disturbed inflow case are smaller in the wake region of the blade.

The visualization of the instantaneous flow field is shown in Fig. 10, where the coherent structure is identified using the Q-criterion and rendered in streamwise velocity. The effect of disturbed inflow can be qualitatively illustrated in this figure. It can be appreciated that the uniform inflow case sheds coherent large-scale vortical structures from the trailing edge, while the disturbed inflow modifies the transition mechanism for which the TS wave is no longer available and therefore it prohibits the formation of Karman vortex shedding and increases the content of small coherent structures in the wake of the blade. Subsequently, the separation bubble is closed before the trailing edge in the disturbed inflow case otherwise open in the uniform case, which is very similar to that observed in Cassinelli et al. [23].

5 Conclusion

In the present study, a high-fidelity Fourier-spectral element method is employed to numerically investigate the aerodynamic characteristics of T106A turbine cascade at moderate *Re*. Two different inflow conditions, including uniform inflow and disturbed inflow, are adopted and for the latter a small circular cylinder is placed upstream side of the cascade to generate wake turbulence. Basic characteristics of flow separation and transition are analyzed in detail and compared for the two cases. The main conclusions obtained are as follows:

The numerical results show that the spectral/*hp* element method can accurately predict the flow separation and transition performance of low-pressure turbine cascades even at lower polynomial order, which is verified in good agreement with the numerical results at higher polynomial order in Cassinelli et al. [23].

It is found that the wake-type inflow turbulence due to the presence of small cylinder upstream of the cascade provides physical disturbance to modify the flow dynamics in the boundary layer of the blade in terms of pressure and skin friction coefficient, boundary layer parameters, wake pressure loss coefficient as well. The turbulence incoming flow reduces the skin friction coefficient in the front portion of the suction surface with respect to the uniform inflow case. This observation is in contrast with the body-forcing disturbance reported in Cassinelli et al. [25]. The probable reason may be the modification of the pressure distribution in the favorable gradient region.

The time- and spanwise-averaged statistics of pressure and Reynolds stress and instantaneous wake field also qualitatively reveal the effect of the small cylinder disturbance. More importantly, the wake-type turbulence upstream of the blade breaks down the transition mechanism rooted in K-H instability before the trailing edge and therefore facilitates the boundary layer reattachment and formation of closed separation bubble before the trailing edge.

6 Nomenclature

C, C_{ax} True and axial chord length
C_f, C_p Skin friction and pressure coefficient
H Shape factor
L_z Spanwise domain
U_∞ Reference speed
Re Reynolds number
$\hat{x}$,$\hat{y}$ Normalized axial and vertical distance from the trailing edge
θ Momentum thickness
τ_w Wall shear stress
F Dimensionless frequency
T Dimensionless period
p Skin static pressure on the blade surface
p_{t1} Total inlet pressure
p_{t2} Outlet static pressure
s, S_0 Blade surface distance and total distance

7 Acronyms

DNS Direct numerical simulation
LPT Low Pressure Turbine
LE, TE Leading and Trailing Edge

Acknowledgements
Not applicable.

Authors' contributions
HZ and XP carried out the simulation, and HZ was responsible for writing this manuscript. YB is the corresponding author of this paper who gave instructions on key points of the research. HX guided the overall scheme of this research, and checked and modified the paper. All the authors read and approved the final manuscript.

Funding
This research is financially supported by the National Numerical Wind-tunnel Project (No. NNW2019ZT4-B09).

Availability of data and materials
The data and materials that support the findings of this study are available from the corresponding author upon reasonable request.

Declarations

Competing interests
The authors declare that they have no competing interests.

Author details
[1]School of Naval Architecture, Ocean and Civil Engineering, Shanghai Jiao Tong University, Shanghai 200240, China. [2]AECC Sichuan Gas Turbine Establishment, Mianyang 621000, China. [3]Inner Mongolia Road and Bridge Group Co., Ltd, Huhhot 010000, China. [4]School of Aeronautics and Astronautics, Shanghai Jiao Tong University, Shanghai 200240, China.

Received: 15 October 2021 Accepted: 19 January 2022
Published online: 15 March 2022

References

1. Pfeil H, Herbst R, Schröder T (1983) Investigation of the laminar-turbulent transition of boundary layers disturbed by wakes. J Eng Power 105(1):130–137. https://doi.org/10.1115/1.3227373
2. Hodson HP (1984) Boundary layer and loss measurements on the rotor of an axial-flow turbine. J Eng Gas Turbines Power 106(2):391–399. https://doi.org/10.1115/1.3239576
3. Mayle RE (1991) The 1991 IGTI scholar lecture: the role of laminar-turbulent transition in gas turbine engines. J Turbomach 113(4):509–536. https://doi.org/10.1115/1.2929110
4. Halstead DE, Wisler DC, Okiishi TH, Walker GJ, Hodson HP, Shin H-W (1997) Boundary layer development in axial compressors and turbines: part 2 of 4—compressors. J Turbomach 119(3):426–444. https://doi.org/10.1115/1.2841142
5. Stadtmüller P, Fottner L (2001) A test case for the numerical investigation of wake passing effects on a highly loaded LP turbine Cascade blade. Proceedings of the ASME Turbo Expo 2001: Power for Land, Sea, and Air. Volume 1: Aircraft Engine; Marine; Turbomachinery; Microturbines and Small Turbomachinery. New Orleans, Louisiana, USA. June 4–7, 2001. 2001-GT-0311. https://doi.org/10.1115/2001-GT-0311
6. Sandberg RD, Pichler R, Chen L (2012) Assessing the sensitivity of turbine Cascade flow to inflow disturbances using direct numerical simulation. Paper presented at the 13th International Symposium for Unsteady Aerodynamics, Aeroacoustics and Aeroelasticity in Turbomachinery (ISUAAAT), Tokyo, Japan, 11-14 September 2012
7. Michelassi V, Chen L, Pichler R, Sandberg RD (2014) Compressible direct numerical simulation of low-pressure turbines–part II: effect of inflow disturbances. J Turbomach 137(7):071005. https://doi.org/10.1115/1.4029126
8. Rai MM (2006) Direct numerical simulation of transitional and turbulent flow on a turbine airfoil. 42nd AIAA/ASME/SAE/ASEE Joint Propulsion Conference & Exhibit, Sacramento, California, 9-12 July 2006. AIAA 2006-4460. https://doi.org/10.2514/6.2006-4460
9. Lombard JEW, Moxey D, Sherwin SJ, Hoessler JFA, Dhandapani S, Taylor MJ (2016) Implicit large-eddy simulation of a wingtip vortex. AIAA J 54(2):506–518. https://doi.org/10.2514/1.J054181
10. Vermeire BC, Witherden FD, Vincent PE (2017) On the utility of GPU accelerated high-order methods for unsteady flow simulations: a comparison with industry-standard tools. J Comput Phys 334:497–521. https://doi.org/10.1016/j.jcp.2016.12.049
11. Moura RC, Sherwin SJ, Peiró J (2015) Linear dispersion-diffusion analysis and its application to under-resolved turbulence simulations using discontinuous Galerkin spectral/*hp* methods. J Comput Phys 298:695–710. https://doi.org/10.1016/j.jcp.2015.06.020
12. Nakhchi ME, Naung SW, Rahmati M (2020) DNS of secondary flows over oscillating low-pressure turbine using spectral/hp element method. Int J Heat Fluid Flow 86:108684. https://doi.org/10.1016/j.ijheatfluidflow.2020.108684
13. Wu X, Durbin P (2001) Evidence of longitudinal vortices evolved from distorted wakes in a turbine passage. J Fluid Mech 446:199–228. https://doi.org/10.1017/S0022112001005717
14. Wissink JG (2003) DNS of separating, low Reynolds number flow in a turbine cascade with incoming wakes. Int J Heat Fluid Flow 24(4):626–635. https://doi.org/10.1016/S0142-727X(03)00056-0
15. Xu H, Cantwell CD, Monteserin C, Eskilsson C, Engsig-Karup AP, Sherwin SJ (2018) Spectral/*hp* element methods: recent developments, applications, and perspectives. J Hydrodyn 30(1):1–22. https://doi.org/10.1007/s42241-018-0001-1
16. Karniadakis GE, Israeli M, Orszag SA (1991) High-order splitting methods for the incompressible Navier-Stokes equations. J Comput Phys 97(2):414–443. https://doi.org/10.1016/0021-9991(91)90007-8
17. Guermond JL, Shen J (2003) Velocity-correction projection methods for incompressible flows. SIAM J Numer Anal 41(1):112–134. https://doi.org/10.1137/S0036142901395400
18. Karniadakis G, Sherwin S (2005) Spectral/hp element methods for computational fluid dynamics, 2nd edn. Oxford University Press, Oxford
19. Dong S, Karniadakis GE, Chryssostomidis C (2014) A robust and accurate outflow boundary condition for incompressible flow simulations on severely-truncated unbounded domains. J Comput Phys 261:83–105
20. Geuzaine C, Remacle JF (2009) Gmsh: A 3-D finite element mesh generator with built-in pre- and post-processing facilities. Int J Numer Methods Eng 79(11):1309–1331. https://doi.org/10.1002/nme.2579
21. Georgiadis NJ, Rizzetta DP, Fureby C (2010) Large-eddy simulation: current capabilities, recommended practices, and future research. AIAA J 48(8):1772–1784. https://doi.org/10.2514/1.J050232
22. Kirby RM, Sherwin SJ (2006) Stabilisation of spectral/*hp* element methods through spectral vanishing viscosity: application to fluid mechanics modelling. Comput Methods Appl Mech Eng 195(23-24):3128–3144
23. Cassinelli A, Montomoli F, Adami P, Sherwin SJ (2018) High fidelity spectral/hp element methods for turbomachinery. Proceedings of the ASME Turbo Expo 2018: Turbomachinery Technical Conference and Exposition. Volume 2C: Turbomachinery. Oslo, Norway. June 11–15, 2018. GT2018-75733. https://doi.org/10.1115/GT2018-75733
24. Denton JD (1993) The 1993 IGTI scholar lecture: loss mechanisms in turbomachines. J Turbomach 115(4):621–656
25. Cassinelli A, Xu H, Montomoli F, Adami P, Diaz RV, Sherwin SJ (2019) On the effect of inflow disturbances on the flow past a linear LPT vane using spectral/hp element methods. Proceedings of the ASME Turbo Expo 2019: Turbomachinery Technical Conference and Exposition. Volume 2C: Turbomachinery. Phoenix, Arizona, USA. June 17–21, 2019. GT2019-91622. https://doi.org/10.1115/GT2019-91622

Publisher's Note